Disruptive Burning of Precursor/Solvent Droplets in Flame-Spray Synthesis of Nanoparticles

Christopher D. Rosebrock, Norbert Riefler, Thomas Wriedt, and Lutz Mädler
Dept. of Production Engineering, Foundation Institute of Materials Science (IWT), University of Bremen, 28359 Bremen, Germany

Stephen D. Tse
Dept. of Mechanical and Aerospace Engineering, Rutgers, The State University of New Jersey, Piscataway, NJ 08854

DOI 10.1002/aic.14234
Published online October 4, 2013 in Wiley Online Library (wileyonlinelibrary.com).

Flame spray pyrolysis is an established technique for synthesizing nanoparticles in the gas phase through aerosol combustion of precursor/solvent droplets. The combustion characteristics of isolated micron-sized precursor/solvent droplets are investigated experimentally. Pure solvent droplets burn uniformly and classically quasisteady, whereas precursor/solvent droplets manifest disruptive combustion behavior. The fast onset of droplet disruption, which occurs only for solutions with dissolved metal precursors, is not due to solid-particle precipitation within the droplet. Instead, the mechanism of disruptive droplet burning is similar to that of slurry droplets, consisting of three main steps: (1) diffusion-controlled burning of the high-volatile solvent, (2) viscous-shell formation due to decomposition of the low-volatile metal precursor, and (3) subsequent disruption due to heterogeneous nucleation. The time sequence of the three steps depends on the concentration and decomposition characteristics of the metal precursor, shortening with increased concentration and higher incremental decomposition temperature. © 2013 American Institute of Chemical Engineers *AIChE J*, 59: 4553–4566, 2013

Keywords: droplet combustion, disruptive burning, decomposition, flame synthesis, flame spray pyrolysis

Introduction

The combustion of liquid fuels occurs in various applications ranging from automotive engines, aircrafts, and steam generators, to material processes such as glass, carbon black, and ceramic production. The latter has received considerable attention in recent years due to the capability of inexpensively producing nanoparticles of high purity and controlled size distributions.[1] One of these production methods is flame spray pyrolysis (FSP), which has become a versatile and scalable technique for synthesizing nanopowders.[2,3] The FSP process involves atomization of a metal precursor/solvent solution with oxidizer in a twin fluid nozzle, resulting in a spray flame with nanoparticle formation due to pyrolysis of the metal precursor and its subsequent oxidation at high temperatures. Thorough reviews of FSP have been presented by Teoh et al.[4] and Strobel and Pratsinis.[5] Key physicochemical mechanisms of particle formation in flames have been deduced from experiments;[6,7] however, mechanistic understanding of the pathways from precursor droplet to final product still needs further investigations. The strong interactions between the droplets in the spray flame, for example, droplet collision and group combustion behavior, make the problem experimentally very challenging to trace and to detect possible reaction and particle formation routes inside and outside the droplet .[3,8,9] To gain more insights, detailed studies during the combustion of precursors and solvents are required. Such investigation can be accomplished with the aid of simulations, which for given aspects can agree reasonably well with experimental FSP results.[10–12] However, due to the aforementioned interactions in the flame spray, simulations will need to treat the droplet-to-nanoparticle-formation process. Depending on the properties of the solvent and metal precursor,[8,13,14] the solvent/precursor droplets can undergo different pathways before reaching the final product particle size, composition, and morphology.[5] Although fine dense nanoparticles are formed by vapor-phase nucleation, inhomogeneous hollow and coarse nanoparticles, which are generally an undesired product, will be favored by precursor decomposition and surface precipitation in the droplets.

Since the seminal publications,[15–18] study of the spherically symmetric burning droplet has served as an invaluable tool for understanding the physical processes of spray combustion and its applications.[19–21] Although droplet regression can follow the classical d^2-law under normal gravity, natural convection can distort the spherical flame shape and therefore negate the simplified spherical symmetry,[22] affecting

Additional Supporting Information may be found in the online version of this article.

Correspondence concerning this article should be addressed to L. Mädler at lmaedler@iwt.uni-bremen.de.

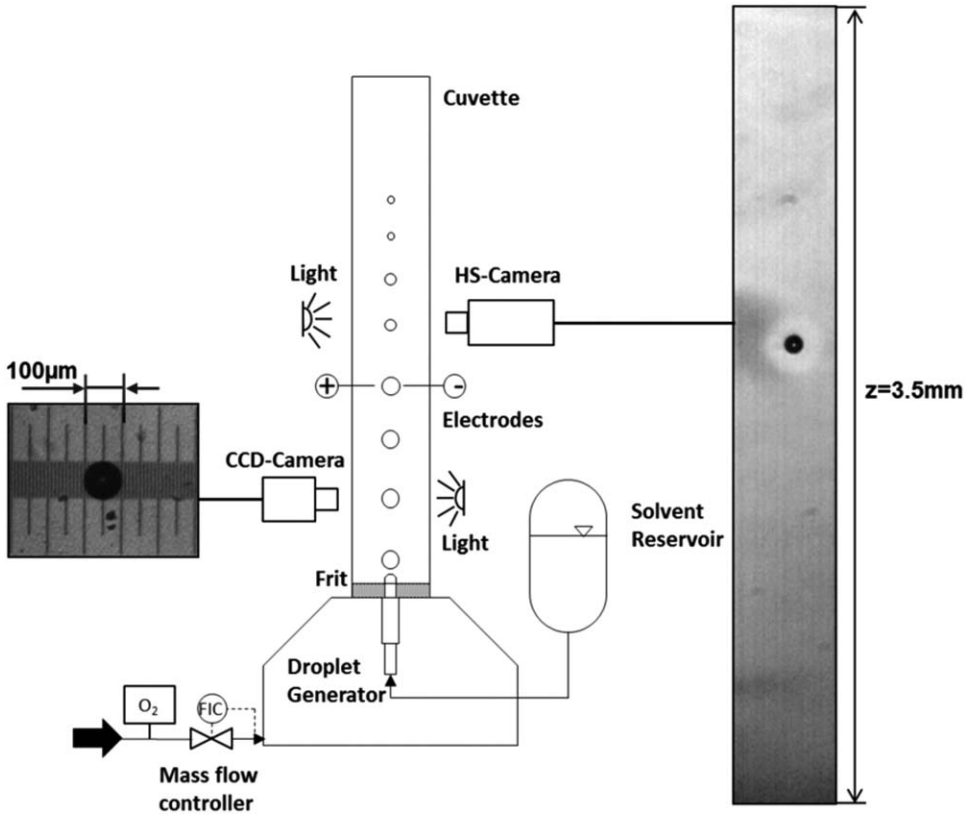

Figure 1. Experimental setup showing droplet generator supplied by a solvent reservoir with xylene, ethanol, heptane, dodecane, or precursor solutions.

The droplet (e.g., 100 μm) is ejected into the coflowing oxygen and traverses the field-of-view of the Charge-Couple-Device (CCD) camera. After the ignition by spark from the electrodes, the combustion is monitored with a high-speed camera up to a distance of z=3.5mm.

burning rate behavior. Nevertheless, there exist certain conditions, where the length scales (and corresponding Grashof numbers) are considerably reduced—for example, a micron-sized droplet burning in an environment of increased oxygen concentration (which keeps flame sizes small)—that favors the spherical flame shape.[23–26]. The FSP process involves atomization of the precursor/solvent into micron-sized droplets using oxygen as dispersion gas. These droplets can burn initially in a pure oxygen atmosphere with subsequent air/product entrainment due to jet mixing. Therefore, single droplet experiments are practically well-suited for fundamental investigation of the droplet-to-nanoparticle-formation mechanisms for the FSP process. Given a lack of such investigations on FSP-type precursor/solvent solutions, it is unknown how their burning behavior will compare to multicomponent fuel droplets previously studied in the combustion literature.

Baseline experiments are conducted with single droplets of pure xylene, ethanol, heptane, and dodecane (which are important FSP solvents), burning in a pure oxygen atmosphere (which has received limited attention in combustion studies). Spherical droplet combustion is observed, with droplet regression following the classical d^2-law. Added to theses solvents, different precursors are investigated, for example, for those forming SnO_2, Cr_2O_3, and CeO_2 nanoparticles. The aerosol combustion dynamics of precursor/solvent droplets may not be necessarily characterized by the distillation limit mode, that is, preferential vaporization of the high volatile component. Instead, disruptive burning may occur, where decomposition characteristics of the precursor play a major role by forming a partially impermeable encapsulating shell, which is promoted by increasing solvent viscosity.

Experimental Layout

Experiments are conducted in a 10 x 10 x 40 mm (L x W x H) orthogonal parallel-piped cuvette as shown schematically in Figure 1. Isolated monodisperse droplets are produced with a piezoelectric generator (piezodropper)[27,28] at a frequency of 4 Hz. The separation distance of two successive d_0=100 μm droplets is s=1875 d_0, which diminishes droplet interference that would otherwise occur for $s \ll 100\ d_0$ in normal air[29] and elevated oxygen concentrations.[30] Therefore, the droplet combustion can be regarded as singular and isolated. The investigated solvents, listed in Table 1, are supplied from a small reservoir to the piezodropper, which ejects the droplets upward through a 2-mm gap between two 100-μm diameter tungsten electrodes, which ignite the droplets by means of a synchronized spark. To reduce deviations in droplet trajectory and surface oscillations,[31] the energy and duration of the spark are minimized for ignition. Save for a very brief transient, the ignition process does not affect the ensuing combustion dynamics. The coflow consists of oxygen (99.95 vol %), which is regulated between 0−2 L/min with a mass flow controller (Bronkhorst—EL-Flow) and is made uniform with a porous frit (ROBU—Glasfilter) before entering the cuvette, preventing fluctuations in the droplet trajectory and establishing plug flow conditions (Figure 1).

The combustion events are recorded with a high-speed camera (IDT—Motion Pro Y4L) at 32,200 fps. Droplet

Table 1. Physical Properties of Liquids Investigated

Liquid	Boiling Point (°C)	Water Solubility (g/kg) (25°C)	Heat of Vaporiztaion (kJ/kg) (25°C)
m-Xylene	139	0.0161	401.75
Ethanol	78	Completely miscible	918.6
Heptane	98	0.00024	364.97
Dodecane	216	0.0000004	361.18
2-Ethylhexanoic acid	228	0.063	524.23

Physical properties are taken from the Handbook of Chemistry and Physics.[80]

diameter, velocity, and flame shape are measured offline using a MatLab-based program, which locates the edges of the droplet (and flame) using a grayscale threshold above the background. The software calculates an average diameter of the horizontal and vertical dimensions of the droplet and compares the position of the center point of successive images to determine local velocity. The final conversion from pixel to micrometer is obtained using a microscope scale (reticle) at a fixed magnification (comparable to Figure 1). The average uncertainty is $1\ \text{pixel} = \pm 3.5\ \mu\text{m}$.

The different liquid precursors dissolved in xylene (VWR, >98% purity) are: Sn(II)2-ethylhexanoate (STREM Chemicals, 90% in 2-ethylhexanoic acid), Cr(III)2-ethylhexanoate (STREM Chemicals, 70% in 2-ethylhexanoic acid), and Ce(III)2-ethylhexanoate (Alfa Aesar, 49% in 2-ethylhexanoic acid), at different amounts to give molar ratios of 0.1, 0.5, and 1 mol/L. Additional experiments employ dodecane (Sigma Aldrich, >99.5% purity) as solvent for a 0.1 mol/L solution of Ce(III)2-ethylhexanoate. Table 1 gives the physical properties of these liquids. Note that due to the lack of physical properties for the 2-ethylhexanoate-based precursors, Table 1 lists only 2-ethylhexanoic acid, which is the major constituent of the 2-ethylhexanoate-based solutions.

Results and Discussion

Spherical droplet combustion

Figure 2 shows a sequence of high-speed camera images for a 112 μm xylene droplet burning in oxygen coflowing at $0.4\ \text{L/min}$. Upon spark igniting of the droplet, a spherical diffusion flame forms, as can be seen from the second and third droplet images in Figure 2. The spherical flame shape is maintained at all times while the flame is visible in the experiment. The stochastic nature of the ignition spark introduces differences in the onset of ignition for each droplet. Nevertheless, with appropriate time shifting, Figure 3 (which shows data for three burning xylene droplets at initially different distances to the igniting spark) confirms that the droplets burn equivalently. Figure 3a shows the evolution of the droplet and flame diameters during combustion, and Figure 3b presents the droplet velocities. Note that in many cases the contrast between the droplet and ambient is not resolvable for $d_p < 20\ \mu\text{m}$. Also, the flame has a lower contrast compared to the droplet, and the amount of soot produced diminishes as the droplet size decreases.[30] Thus, it is not possible to resolve the flame for $d_f < 200\ \mu\text{m}$ (compare Figure 2). Nonetheless, Figure 3a shows that, if measurable, the flame diameters also coincide. The velocities, however, deviate a bit more among the three droplets (see Figure 3b). These small differences in the velocity between the different ignition points can be attributed to the transferred momentum of the induced shock wave of the spark, which is higher if the droplet is beyond and close to the spark. Still, the different droplet velocities are comparable to each other, so that despite small differences in the onset of ignition, the combustion can be regarded as temporally and spatially reproducible.

The classical quasisteady (CQS) approximation for droplet combustion, termed the d^2-law, is characterized by the following features: (1) the square of the droplet diameter (which is proportional to surface area) decreases linearly with time; (2) the flame front standoff ratio, defined as the ratio of the flame radius to the droplet radius, is constant; (3) the flame temperature is constant; and (4) flame burnout is coincident with complete droplet consumption. Oftentimes, the first feature is readily satisfied (as it is for our results—see Figure 6), while aspects related to the flame radius and shape may not be. If the flame is spherical and concentric to the droplet, Miyasaka and Law[23] pointed out that buoyancy effects can be neglected. Figure 4 displays the ratios of the x and y center coordinates of the flame and droplet. The lines in Figure 4 represent the individual images seen in Figure 2, where the spherical flame starts to form around the first dashed line and is not resolvable beyond the second dashed line. Figure 4 shows that the origins of the flame and droplet coincide almost exactly while the flame is resolvable. The deviation between $t=2.4$ ms and $t=7.5$ ms is within a 2% range. Furthermore, $Gr \approx O\left(10^{-4}\right)$ for our setup, supporting that buoyancy effects can be neglected.[32] These results illustrate spherical burning for our experiments.

Up to this point, only droplets burning in coflowing oxygen with a constant mean velocity have been considered ($v_{\text{amb}} = 0.067\ \text{m/s}$). To examine the possible role of forced convection, experiments are conducted with different initial droplet momentum (where impulse can be controlled with the droplet generator) and ambient flow rates. Figure 5a shows the average droplet and flame diameters for two different droplet momenta and oxygen flow rates. Figure 5b shows their corresponding droplet velocities, along with the flame-to-droplet diameter ratio. As seen from Figure 5b, droplets with different initial momenta have different initial droplet velocities, that is, $v_p = 1.1\ \text{m/s}$ and $v_p = 0.75\ \text{m/s}$. A higher oxygen flow rate ($v_{\text{amb}} = 0.267\ \text{m/s}$) with constant initial momentum reduces the deceleration due to the decreasing relative velocity between the ambient and the droplet, so that the droplet velocity is slightly higher (see Figure 5b).

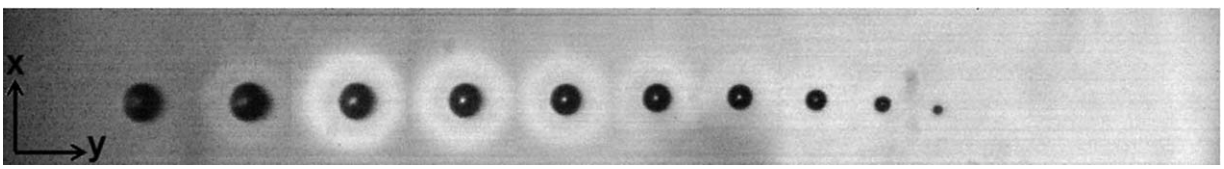

Figure 2. Image sequence of a 112μm xylene droplet burning in oxygen coflowing at 0.4 L/min.

The time interval between each droplet image is 0.8385 ms.

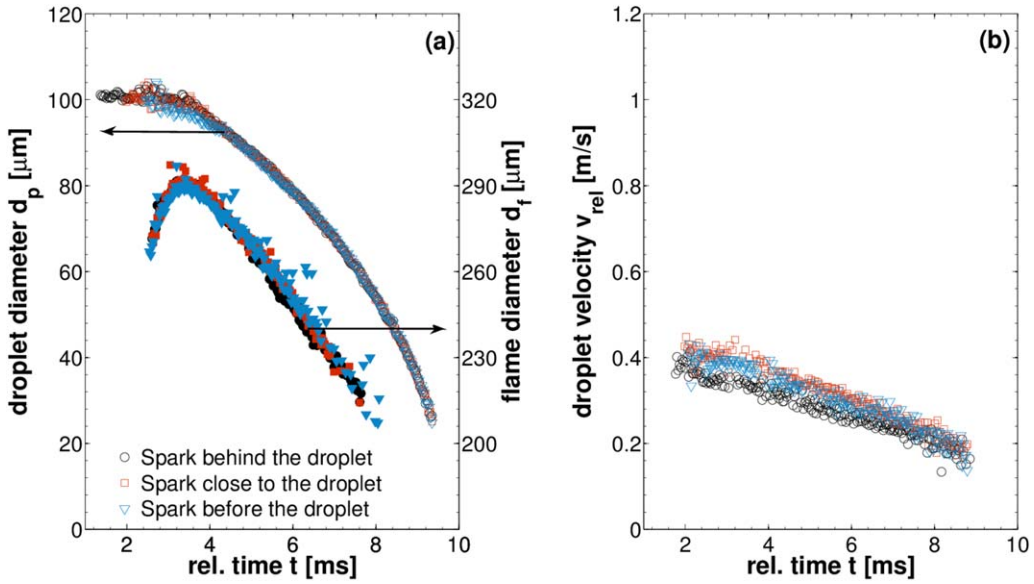

Figure 3. Evolution (time shifted) of (a) the droplet and flame diameters, and (b) droplet velocity, for three xylene droplets with different ignition points, at 0.4 L/min coflowing oxygen.

[Color figure can be viewed in the online issue, which is available at wileyonlinelibrary.com.]

However, the droplet and flame diameters in Figure 5a show no significant differences, except that the high momentum droplets exit the observation window before combustion completes. Parenthetically, this is the reason for the limited data points of the high momentum droplet, ending at $t=6.7$ ms. The slightly earlier onset of the flame at high momentum is attributed to the increased relative velocity between the ambience and the droplet, which results in faster attainment of a flammable mixture due to mixing.[33,34]

Because pure oxygen constitutes the ambient atmosphere, such that the flame size is small, it is also expected that the instantaneous flame-to-droplet diameter ratio should attain a constant value, suggesting a CQS process.[24] However, Figure 5b shows that the ratio varies as combustion proceeds. Although gas-phase quasisteadiness may still be valid, with respect to the reference frame of the moving flame as given in He et al.,[35] the ignited flame is situated initially very close to the droplet surface and does not correspond to the CQS flame position. As such, the fuel mass consumption rate at the flame is smaller than the fuel vaporization rate at the droplet surface, causing the flame to spread accordingly, such that the ratio is not constant. Moreover, He et al.[35] give a criterion where the CQS theory holds (for flame to droplet diameter ratio), that is, the quasisteady parameter $Q_s=\rho r_f^3/\rho_l r_l^3 \ll 1$, where ρ, ρ_l is the gas and liquid density and r_f, r_l flame and droplet radius, respectively. Since $\rho/\rho_l \sim 10^{-3}$ for xylene, $Q_s \sim 10^{-1}$, which although small, is about an order of magnitude larger than that needed (as found by Ref. 35) for the ratio to remain constant, even for a flame initially starting at the CQS position. Therefore, the flame-to-droplet diameter ratio is not constant, and the CQS theory not completely fulfilled.

Xylene has a high sooting tendency due to its benzene ring, which may easily form polycyclic-aromatic hydrocarbons, the

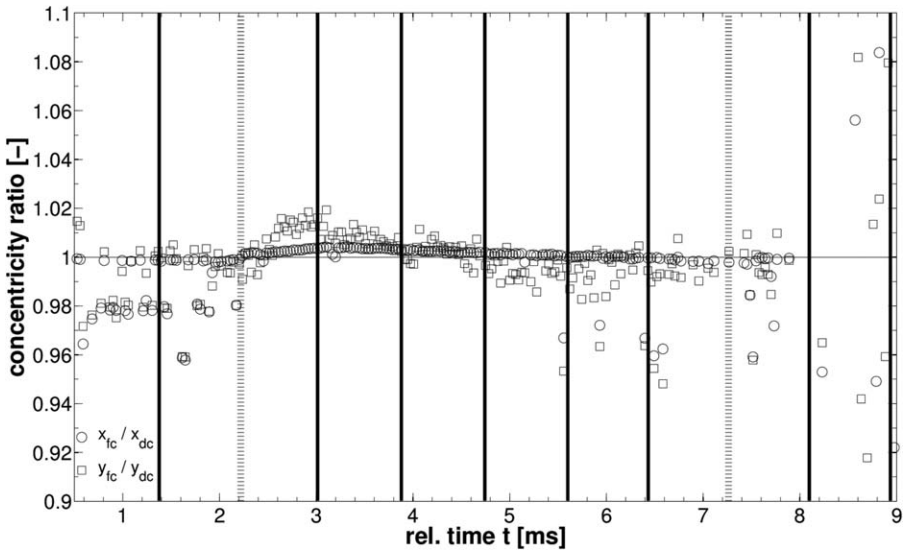

Figure 4. Concentricity ratio of the *x* and *y* center coordinates of the flame and droplet circumference for a 112-μm xylene droplet from Figure 2.

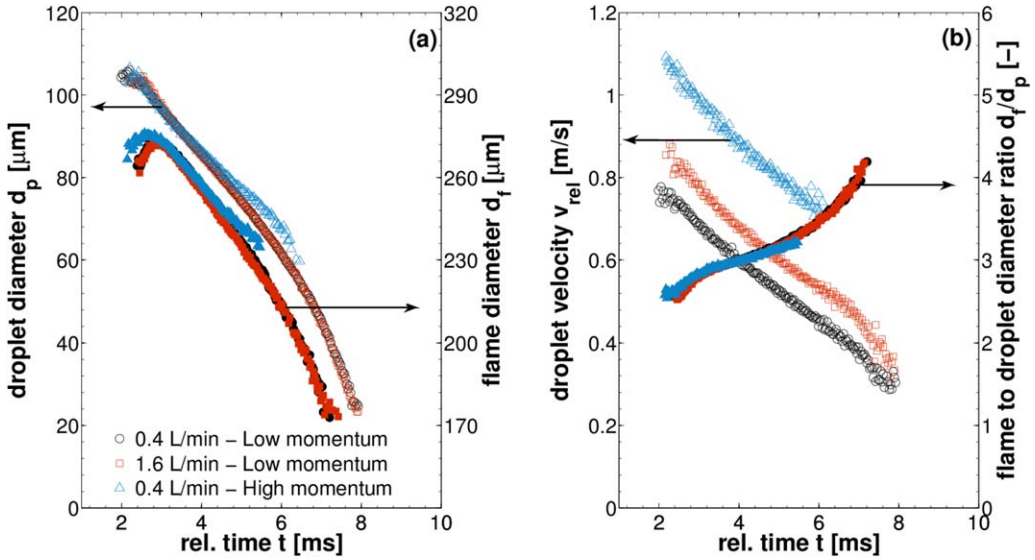

Figure 5. Evolution (time shifted) of (a) the average flame and droplet diameters and (b) the droplet velocity and flame-to-droplet diameter ratio, for xylene droplets with different initial momenta and coflowing oxygen rates.

[Color figure can be viewed in the online issue, which is available at wileyonlinelibrary.com.]

major precursors for soot.[36,37] Soot formation can reduce the flame temperature due to high endothermic reaction and radiative loss. It can also act as a diffusion barrier for xylene transport to the flame front, thereby decreasing the reaction rate and subsequently increasing the fuel accumulated between the droplet and the flame. Table S1, where calculated burning constants of different pure solvents are presented (see Supporting Information), which are the slopes of the linear

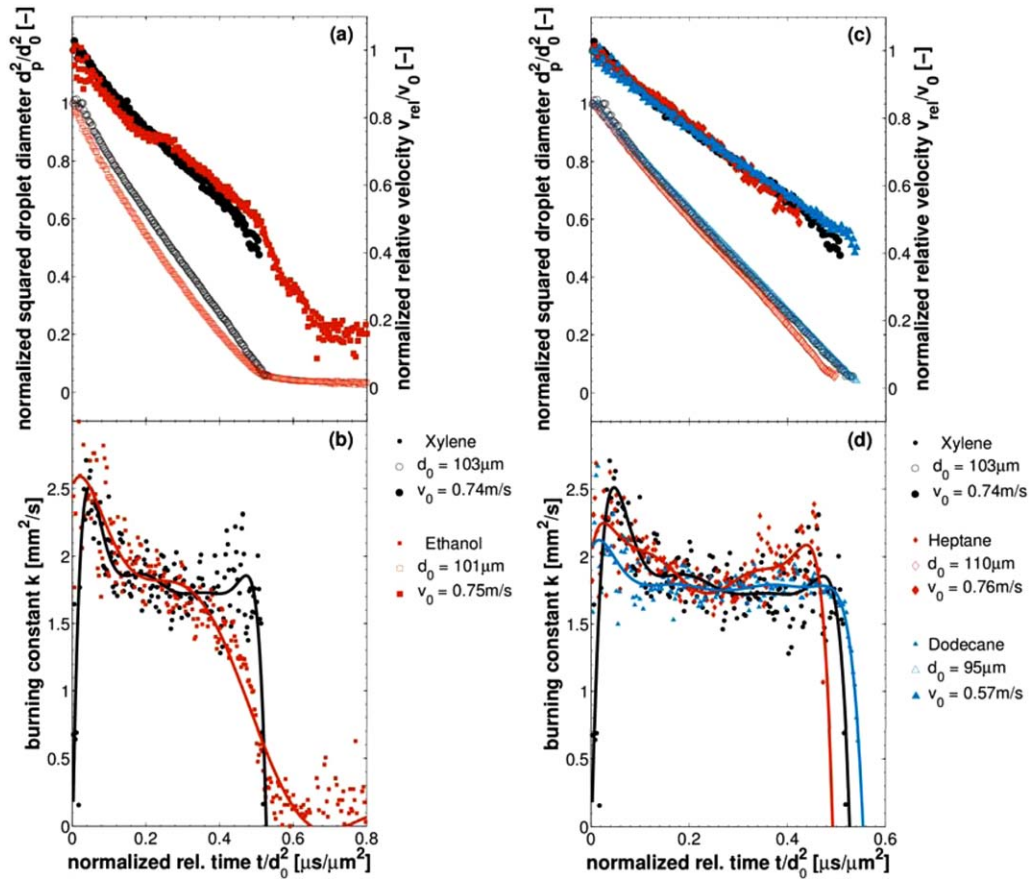

Figure 6. Evolution of (a) averaged normalized droplet diameter and velocity and (b) burning constant, for pure xylene and ethanol.

Evolution of (c) normalized droplet diameter and velocity and (d) burning constant, for pure xylene, heptane, and dodecane burning in 0.4 L/min coflowing oxygen. d_0 is the initial droplet diameter, and v_0 is the initial velocity. [Color figure can be viewed in the online issue, which is available at wileyonlinelibrary.com.]

decreasing squared droplet diameters, shows that xylene differs noticeably from its experimental value, in comparison to the other pure fuels. Law and Williams[32] attributed this deviation to reaction kinetic effects, in agreement with many investigations regarding soot formation during droplet combustion,[39–45] where reduced burning rates are observed for high soot content. The other solvents examined in this work are much less sooty (such that the flame is often not visible); nevertheless, adherence to the CQS behavior will ultimately be based on the flame size, whereby $Q_s \ll 1$. Notwithstanding, the burning process can still be described by gas-phase quasisteadiness, when accounting for flame front motion;[35] and the combustion of the isolated single droplets in this work are spherical and burn uniformly for all experimental conditions where no droplet disruption is reported.

Combustion of pure solvent droplets

Before the additions of metal-organic precursors to the droplets are discussed, the results for pure solvents are presented. Figures 6a,c show the evolution of the squared droplet diameter (open symbols) along with the corresponding droplet velocities (filled symbols), with both normalized by their initial values, that is, d_0 and v_0, of pure xylene (○), ethanol (□), heptane (◇), and dodecane (Δ), in coflowing oxygen at 0.4 L/min. Figures 6b,d present the burning constant k, which is evaluated using a moving linear regression over five data points and subsequently differentiated with respect to time. For better visualization only, an eighth-order polynomial is fitted to the experimental data points. Because only xylene seems to generate enough soot for a visible flame, the evolutions of the flame diameter, if not explicitly mentioned, are not presented.

As can be seen from Figures 6a,c, nearly all solvents follow the classical d^2-law for droplet size regression. However, ethanol shows a slight curvature in the plot of squared droplet diameter as a function of time, flattening out at $t/d_0^2 = 0.52 \ \mathrm{s}/\mu\mathrm{m}^2$, which corresponds to flame extinction prior to complete droplet consumption. Differences with the other solvents also exist for the velocity, where ethanol does not exhibit the approximately linear decay trend as characterized by the other solvents (see also Figure 6c). Obviously, the velocity of the ethanol droplet dips at the onset of extinction. In addition, ethanol exhibits a short period of nearly constant velocity at $t/d_0^2 = 0.22 \ \mathrm{ms}/\mu\mathrm{m}^2$, which along with subsequent extinction, can be attributed to its different water solubility and boiling point compared to those for other solvents (Table 1). With water vapor being a major product of combustion, high water vapor concentration in the reaction zone produces a diffusion flux toward the droplet surface. The higher boiling point of water will lead to condensation of water onto the droplet surface, dissolving into the ethanol droplet. As shown by Law et al.[46] and Lee and Law,[47] the condensation of water first increases the vaporization rate of the low-volatile fuel due to the release of latent heat of the water. However, as the amount of dissolved water continuously increases during the burning, the fuel concentration present at the droplet surface is reduced. This in turn decreases the amount of vaporized fuel and subsequently extinguishes the combustion due to reduced heat release in the reaction zone. Indeed, the burning constant of ethanol, as shown in Figure 6b, displays such staged behavior. Like the other solvents, it first increases due to the ignition, but reaches a slightly higher burning constant than the other solvents due to the latent heat release of water. Later, the burning constant decreases to a short period of nearly constant value, $k = 1.85 \ \mathrm{mm}^2/\mathrm{s}$, because a balance between water accumulation and ethanol vaporization is reached. This short period coincides with that of constant velocity. Finally, the burning constant drops to a minimum value due to the extinction of the droplet. As was shown theoretically and experimentally by Shaw et al.,[48–51] the concentration change in the surface layer (in this case, the increasing amount of water) is accompanied by a flame contraction. Because the drag force exerted on a burning/evaporating droplet is smaller than a solid sphere due to the reduced shear stress from the outwardly directed Stefan flow[52–55] and the transfer of momentum from surface shear into internal circulation of the droplet, the flame contraction seems to correspond to a reduced deceleration of the droplet. For example, as the flame is situated closer to the droplet surface at flame contraction, the vaporization rate may increase due to the improved heat transfer to the droplet surface, reducing the drag force according to $C_D/C_{0D} \propto 1/(1+B_m)$, where C_D and C_{0D} are the drag force coefficient of a burning/evaporating droplet and solid sphere, respectively, and B_m is the mass-transfer number.[15] Although this needs to be further investigated, it might be an adequate measure of changes during droplet combustion if no flame is visible. This could be particularly important for small burning droplets, which lack soot formation, thus making flame visualization more difficult,[40,42] particularly for high-speed camera recordings, which need a high illumination due to the short exposure times of the CCD.

The burning behaviors of xylene, heptane, and dodecane are comparable, as seen in Figure 6c. The surface area of the different solvent droplets decreases linearly, along with their velocity. The similarity is also evident from the burning constants, which show the same trends and values. At the beginning, the burning constants increase due to ignition of the droplets, but soon attain nearly constant values. Because xylene has higher vapor heat conductivity as well as lower liquid specific heat capacity compared to that of heptane and dodecane, the rising peaks of the burning constants of the other solvents are more moderate. The final increase in the burning constants, especially that of heptane, might be due to the decreasing droplet size, which has been observed in the literature.[42,56] Nevertheless, because the resolution of the high speed camera is limited to $d_p < 20 \ \mu\mathrm{m}$, the final increase needs further investigation.

As shown in Figures 6b,d, all pure solvents, except ethanol which decreases to zero after a short period of nearly constant k, attain a nearly constant burning constant value after the initial peak until burnout of the droplet, consistent with the d^2-law. Therefore, calculations are carried out and compared to the experimental and literature data. Because most tabulated burning constants are evaluated while fitting a linear regression to the squared diameter evolution, the burning constants are evaluated with a linear regression of the data points between $d_p^2/d_0^2 = 1$ and 0.1. Table S1 compares the calculated burning constants with the experimental values. Only xylene shows significant deviation, which might be due to its sooting tendency. However, comparing the experimental results with data from the literature, it seems that the burning constants are better represented by Aldred and Williams.[38] Nevertheless, it should be noted that the tabulated burning constant from the literature was measured for relatively-large supported droplets, suggesting natural convection effects, which would increase the burning rate of the fuel and thus the burning constant. Surprisingly, there

seems to be a lack of study of single isolated droplet combustion in pure oxygen for sizes below 100 μm, despite being the typical size range of droplets in sprays.[57]

Combustion of precursor/solvent droplets

Combustion leads to fast vaporization rates, which can result in concentration gradients between the droplet surface and the interior of multicomponent droplets due to slow liquid mass diffusion compared to heat diffusion. If the boiling point temperature of the low-volatile component exceeds the critical vapor nucleation temperature of the high-volatile component, vapor nucleation in the liquid may be initiated, forming vapor bubbles that expand and burst the droplets.[58,59] In the following discussions, "nucleation" refers to "vapor nucleation." FSP typically consists of such multicomponent droplets with a high-volatile solvent and a low-volatile metal precursor, for example, metal 2-ethylhexanoate (2-EH) solutions, which are attractive precursors due to their high solubility, air-stability, nontoxic nature, and price.[61] However, these precursors have large volatility differences with common solvents (e.g., xylene), as the major constituent is the low-volatile 2-ethylhexanoic acid (2-EH acid).

Combustion of Binary Xylene/2-EH Acid Solution

To investigate such droplet disruptions, droplets composed of pure 2-EH acid dissolved in pure xylene are investigated. Here, the same amount of pure 2-EH acid as an equivalent 1 mol/L Sn(II)2-ethylhexanoate in xylene solution would contain is mixed with pure xylene and burned in 0.4 L/min coflowing oxygen. This 2 mol/L 2-EH acid in xylene droplet burns slightly slower than pure xylene (Figure 7a). This effect is also evident from the normalized velocity of the xylene/2-EH acid solution, which decreases initially the same as that for pure xylene, but later maintains higher velocities as combustion proceeds. Because there is a proportionality between velocity and squared droplet diameter, $v_p \propto d_p^2$, in the examined range, the slower combustion of xylene/2-EH acid will decrease the deceleration of the droplet compared to the pure xylene. The burning constant in Figure 7b shows the same trend, being slightly smaller than that for pure xylene. These results imply that the 2-EH acid decelerates the combustion. The normalized squared diameter and velocity evolutions, as well as the burning constant of the xylene/2-EH acid solution do not show droplet disruption, until the very end of the observation limit when the droplet suddenly undergoes microexplosion (marked with an arrow in Figure 7a).

Assuming a well-mixed droplet, the slow burning and the change of the droplet velocity slope at $t/d_0^2 = 0.1\ \mu s/\mu m^2$ are attributed to 2-EH acid accumulation at the droplet surface. During the early combustion stage, both xylene and 2-EH acid are present at the surface. Because 2-EH acid has a higher boiling point and heat of vaporization (Table 1), not all of the incoming energy of the combustion is used to vaporize xylene. Some energy is stored in 2-EH acid to raise its temperature, thus decreasing the amount of vaporized xylene reaching the reaction zone. Subsequently, less energy is released during the reaction, resulting in a slower heat release. Nevertheless, because of its lower boiling point and lower heat of vaporization, xylene has the higher vaporization rate, leading to its surface depletion and an increasing concentration of 2-EH acid. The higher 2-EH acid concentration at the surface decreases the overall vaporization rate, and the reaction zone moves closer to the droplet surface, that is, the flame diameter d_f decreases (see Figure S1 in Supporting Information). As already mentioned, this might cause a reduced deceleration of the droplet. However, liquid diffusion increases with increasing temperature also, so that in conjunction with the concentration gradient between the surface and interior core, the amount of xylene at the surface is rapidly balanced. Zhang and Law,[60] for example, indicated that the liquid Lewis number (the ratio of thermal diffusivity to mass diffusivity) will readily decrease as vaporization is initiated, thus approaching the distillation limit mode. This effect strongly depends on the volatility difference of the components.[60] The higher the volatility difference, the better is the agreement to the distillation limit mode. Because the volatility difference between 2-EH acid and xylene is not extremely large, the droplet burns uniformly without an appreciable concentration gradient. This explains the late

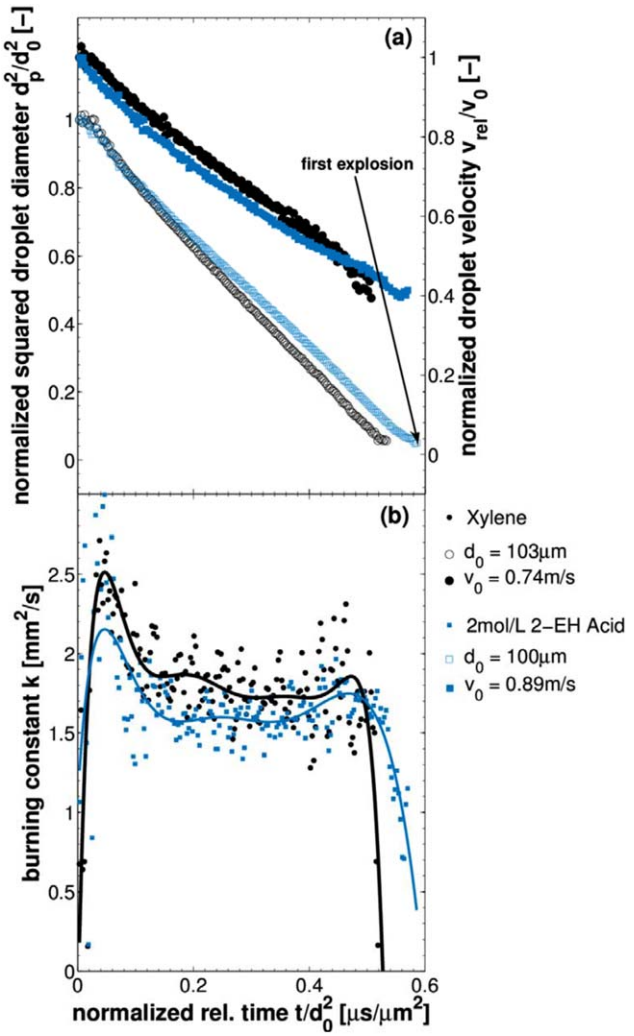

Figure 7. Evolution of (a) averaged normalized droplet diameter and velocity and (b) burning constant, for pure xylene (○) and 2 mol/L 2-ethylhexanoic acid in xylene (□), burning in 0.4 L/min coflowing oxygen.

d_0 is the initial droplet diameter, and v_0 is the initial velocity. [Color figure can be viewed in the online issue, which is available at wileyonlinelibrary.com.]

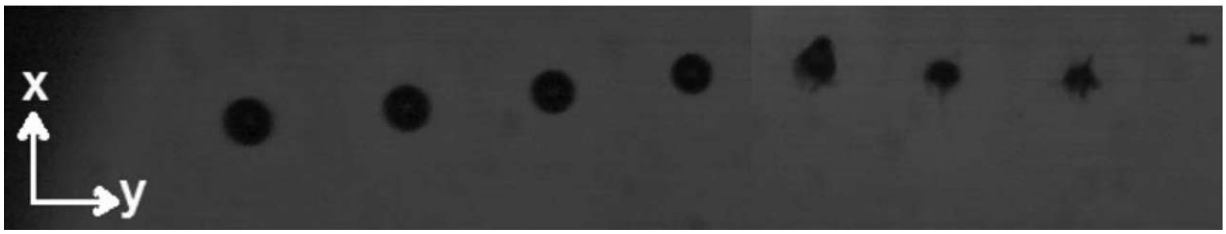

Figure 8. Image sequence of a 100-μm droplet composed of 0.5 mol/L Sn(II)2-ethylhexanoate in xylene burning in 0.4 L/min coflowing oxygen.

The time interval between each droplet image is 621 μs.

disruptions of the droplets at the end, although the homogeneous nucleation temperature of xylene (T_{hn}=235 °C[62]) is close to the boiling point of 2-EH acid (Table 1). Only when almost all xylene is vaporized, then a small residual amount will be superheated, initiating droplet disruption.

Combustion of Binary Xylene/Metal-2-EH Solution

Depending on the volatility difference, metal-2-EH/solvent solutions may lead to droplet disruption. However, the combustion may deviate from that of the binary mixture presented in the preceding section. Figure 8 shows a sequence of images for a droplet (d_P=101 μm) composed of 0.5 mol/L Sn(II)2-ethylhexanoate dissolved in xylene, burning in 0.4 L/min coflowing oxygen. The time interval between each droplet position is Δt=621 μs, and ignition occurs before the first droplet image. The droplet burns initially without any perturbation, with the same combustion behavior as without the metal. However, thereafter the droplet suddenly undergoes disruptions, where parts of the liquid are ejected from the droplet surface. This process continues until the initial droplet is completely consumed. In addition, long segments of the ejected liquid are sometimes observed that retract back into the droplet due to surface tension forces, entrapping ambient gas and leading to more violent droplet disruption. Such an example is shown in Figure 9, as a sequence of images with a time interval of Δt=62 μs. The droplet first starts to eject liquid due to a small disruption on the surface (Figures 9a–d). Due to the retraction of the partially ejected segment, the droplet traps gas (Figures 9d–e), resulting in a first violent disruption (Figure 9f). Subsequently, more gas is trapped, leading to an enlargement of the droplet due to the entrapped bubble (Figure 9g), which further expands and explodes violently with a bright flame (Figures 9h,i). If the droplet does not trap further ambient gas like in Figure 9j, the violent disruptions stop; and the droplet undergoes a cascading series of liquid ejection, similar to that shown in Figure 8. Although both sequences occur given the stochastic nature of ambient gas trapping within the droplet, the sequence in Figure 8 is more frequently encountered (i.e., about 95% of the time). Nevertheless, disruptions for both sequences (Figures 8, 9) have almost the same time delay until onset, being highly reproducible (as seen in the error bars in Figure 14). These observations evince that the combustion behavior of metal-2-EH/solvent solutions is different than that for the binary mixture of pure 2-EH acid in xylene.

Figure 10 shows the normalized diameter and velocity evolutions, along with the burning constants, of droplets composed of different Sn(II)2-EH concentrations dissolved in xylene, as well as of xylene/2-EH acid solution for comparison. Note that frequent disruptions prohibit a proper resolution of droplet size and velocity; and therefore, quantitative analyses cease at the onset of the first disruption, as marked with arrows in Figure 10a. The disruption is also the

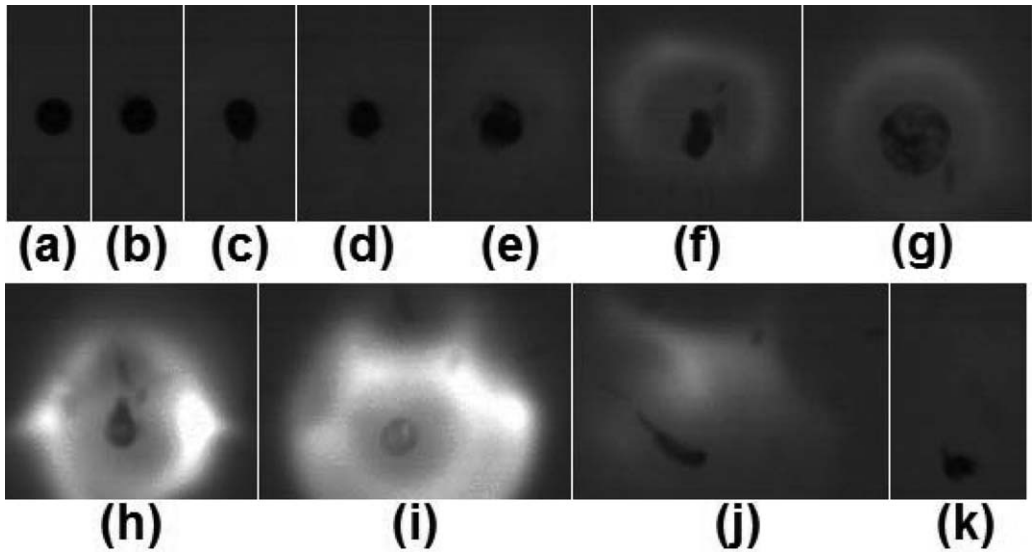

Figure 9. Image sequence of a 101-μm droplet composed of 0.5 mol/L Sn(II)2-ethylhexanoate in xylene, showing trapping of ambient gas during the disruption.

The time interval between each droplet image is 62 μs.

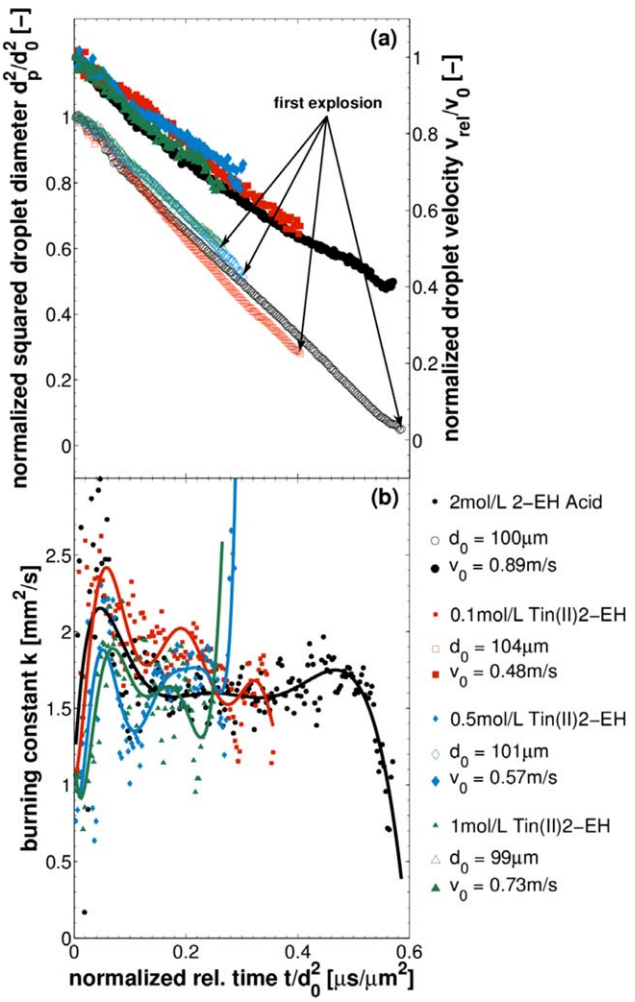

Figure 10. Evolution of (a) averaged normalized droplet diameter and velocity and (b) burning constant, for 2 mol/L 2-ethylhexanoic acid in xylene (○), 0.1 mol/L (□), 0.5 mol/L (◇), and 1 mol/L (Δ) Sn(II)2-ethylhexanoate in xylene burning in 0.4 L/min coflowing oxygen.

d_0 is the initial droplet diameter, and v_0 is the initial velocity. [Color figure can be viewed in the online issue, which is available at wileyonlinelibrary.com.]

reason for the final spike in the "extracted" burning constant (Figure 10b). Figure 10a shows that the Sn(II)2-EH solution experiences disruption much sooner than the solution without the metal. However, the slopes of the droplet surface-area (equal to the burning constants in the d^2-law) and the velocities coincide roughly for both solutions, with and without metal, suggesting similar combustion behavior as expected due to the same amount of 2-EH acid. The burning constant of 1 mol/L Sn(II)2-EH before disruption is close to that of xylene/2-EH acid solution (Figure 10b). As the Sn(II)2-EH concentration decreases, the onset of disruption is delayed, with accelerated burning prior to disruption. For example, 0.5 mol/L Sn(II)2-EH burns longer and attains a slightly higher burning constant (at $t/d_0^2 \approx 0.2\mu s/\mu m^2$) than does 1 mol/L Sn(II)2-EH. Furthermore, the velocity of the 0.5 mol/L Sn(II)2-EH solution is nearly constant around $t/d_0^2 = 0.11 ms/\mu m^2$, coinciding with the first minimum of the burning constant (Figure 10b). This behavior might be similar to that of pure ethanol, suggesting flame contraction (see Figure S1 in Supporting Information) and a change of concentration in the droplet surface layer, after which the burning constant increases again until the disruption. The 0.1 mol/L Sn(II)2-EH solution burns even longer and faster compared to the 0.5 mol/L Sn(II)2-EH solution, prior to disruption (Figure 10a). The burning constant in Figure 10b is higher for lower concentrations and shows a few local maxima and minima before disruption. The 0.1 mol/L Sn(II)2-EH solution behaves similarly as pure xylene, except for the droplet disruption. Because the Sn(II)2-EH concentration is lower than in the 2 mol/L 2-EH acid in xylene solution, it burns faster. However, 2-EH acid has a higher boiling point, so its concentration increases as combustion proceeds, resulting in the varying slope of the burning constant for 2-EH acid in xylene (Figure 10b).

Combustion of Binary Xylene/2-EH Acid Solution with Suspended Nanoparticles

The dissolved metal content alters the combustion behavior of the droplet as compared to the binary mixture of pure components. Increasing the concentration of Sn(II)2-EH in xylene leads to slower burning and earlier disruption of the droplet. Even for the lowest metal precursor concentration, the droplet disrupts much faster than does the xylene/2-EH acid solution (Figure 10). If homogeneous nucleation is the initiator of these disruptions, xylene/2-EH acid would attain the critical nucleation temperature of xylene faster than the 0.1 mol/L Sn(II)2-EH solution would have, due to the larger amount of 2-EH acid. A higher amount of 2-EH acid should result in a faster development of concentration gradients and thus a faster attainment of higher temperatures due to the boiling point difference. However, the times until onset of disruption between cases for 0.1 mol/L Sn(II)2-EH solution and xylene/ 2-EH acid solution are clearly different, thus suggesting another mechanisms, for example, heterogeneous nucleation. Because Sn(II)2-EH is used to produce SnO_2 nanoparticles in FSP, either precipitation of nanoparticles in the liquid occurs or nanoparticles formed in the flame are transported back to the droplet, acting as heterogeneous nucleation seeds at low supersaturations.[63,64] To examine the effect of nanoparticles within the droplets, 0.04 g of SnO_2 nanoparticles are suspended without any surfactant in the xylene/2-EH acid solution. Details of the SnO_2 nanoparticles preparation is described in the Supporting Information. The results (Figures 11a,b) demonstrate that the SnO_2 nanoparticles have almost no influence on the droplet combustion, other than that the onset of droplet disruption occurs slightly sooner for the solution with the suspended nanoparticles as compared to the solution without them. These results suggest that heterogeneous nucleation may only somewhat increase the onset of droplet disruption, but that the rapid disruption of the Sn(II)2-EH solutions should not be attributed to heterogeneous nucleation by nanoparticles inside the droplet.

Decomposition during Combustion of Binary Xylene/ Metal-2-EH Solution

It is known that Sn(II)2-EH starts to decompose below its boiling point of the major constituent 2-EH acid in a two-stage mechanism with the onset of decomposition around 85°C.[65] Although the decomposition of metal 2-EH is very complex and not fully understood,[66,67] solid and gaseous intermediates are known to form.[68,69] Although the gaseous products will burn, the solid intermediates may remain at the

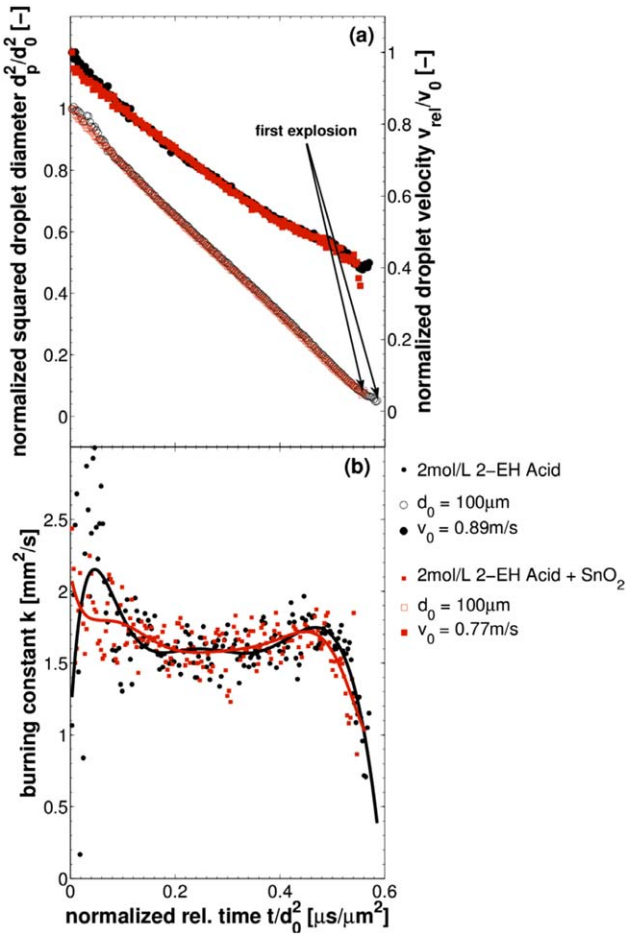

Figure 11. Evolution of (a) averaged normalized droplet diameter and velocity and (b) burning constant, for 2 mol/L 2-ethylhexanoic acid in xylene without (○) and with (□) suspended SnO_2 nanoparticles, burning in 0.4 L/min coflowing oxygen.

d_0 is the initial droplet diameter, and v_0 is the initial velocity. [Color figure can be viewed in the online issue, which is available at wileyonlinelibrary.com.]

liquid surface, accumulating and possibly forming a viscous shell. The evolving shell inhibits further vaporization, and might trap and superheat the high-volatile xylene, thus facilitating droplet disruptions. Comparable observations were also made by Strobel and Pratsinis,[14] who showed that the decomposition of different precursors affects the homogeneity of the nanoparticles produced in FSP. The authors suppose that precipitation due to decomposition leads to in-droplet reactions, forming a shell that densifies at high temperature. These physical mechanisms leading to a viscous shell are similar to the combustion of so-called slurry droplets, which consist of combustible particles suspended in a fuel. Three steps are frequently recognized during the combustion of a slurry droplet, that is, (1) uniform burning of the solvent governed by the d^2-law, (2) shell formation at the droplet surface due to deposition of the suspended particles and decomposition of additives at the droplet surface, and (3) moderate and/or violent disruptions due to nucleation in the shell wall and/or in the superheated liquid encapsulated by the shell, respectively. Takahashi et al.[70,71] observed that the time delay until disruption decreases as the concentration of the surfactant and solid loading increases. Furthermore, they found that the decomposition characteristics of the surfactant influence the time delay until disruption. Similar observations were also made by Wong et al.,[72,73] who showed that slurry droplets, which evaporate at temperatures higher than the decomposition temperature of the surfactant, exhibit strong disruption, whereas evaporation below that temperature decreases the droplet size monotonically. With increasing ambient temperature, increased intensity of droplet disruption has also been observed. Moreover, Wong et al.[73,74] showed that only the addition of low-volatile surfactants in slurry droplets suppressed evaporation, superheating, and heterogeneous nucleation of the carrier fuel. Likewise, Byun et al.,[75] observed a decrease in the vaporization rate and droplet disruption only when surfactant was present in the slurry droplet. These findings are similar to the aforementioned observations of the Sn(II)2-EH and xylene/2-EH acid solution solutions, for example, (1) Sn(II)2-EH solutions burn initially without perturbation (following the d^2-law), but the vaporization rate decreases as the concentration of Sn(II)2-EH increases. (2) It is possible that as combustion proceeds, the low-volatile Sn(II)2-EH accumulates at the droplet surface, heats up, decomposes, and assembles a viscous shell. In agreement with surfactant concentration for slurry fuels, the sequence shortens with increasing concentration of the dissolved Sn(II)2-EH. (3) Finally, as the viscous shell inhibits vaporization, the flame moves closer to the surface (contraction), heating up the shell quickly beyond the heterogeneous nucleation temperature of xylene and 2-EH acid, initiating disruptions. Moreover, disruptions are only observed if Sn(II)2-EH is present, coinciding with the observations of Wong et al.[73,74] and Byun et al.[75] In addition, the disruption may also be initiated by soot or nanoparticles, which are formed in the flame and transported back to the droplet by thermophoresis as proposed by Shaw et al.[31] Very small particles ($d_p \ll 200$ nm) from the gas phase can get close to the droplet surface, as was shown by Ben-Dor et al.[76] The probability of such an effect may increase as the flame contracts due to a decreasing vaporization rate (Figure S1 of Supporting Information), thus reducing the force (i.e., drag force due to the Stefan flow) counteracting thermophoresis. Entrapped ambient gas (Figure 9) may also draw particles into the liquid, where they can act as nuclei.

Combustion of Binary Xylene/Ce(III)2-EH Solution

Experiments are further conducted with different aerosol precursors, which have different decomposition characteristics, but the same carrier liquid, that is, 2-EH acid. Figure 12 shows a sequence of a 97-μm droplet composed of 0.5 mol/L Ce(III)2-EH dissolved in xylene burning in 0.4 L/min oxygen. The time interval between successive images is $\Delta t = 155$ μs. The first image in Figure 12 is one of the undisturbed droplet just prior to disruptive behavior. Figure 12 shows that the 0.5 mol/L Ce(III)2-EH solution droplet burns similarly to the Sn(II)2-EH solution, that is, first without perturbation (not shown) and subsequently with disruption. The Ce(III)2-EH solution droplet continuously deforms until the surface bursts due to bubble growth. Surface tension causes droplet reformation, but the droplet bursts again due to bubble formation. The final residual pyrolysis is characterized by the bright emission in the last image of Figure 12. The disruption caused by a bubble suggests that

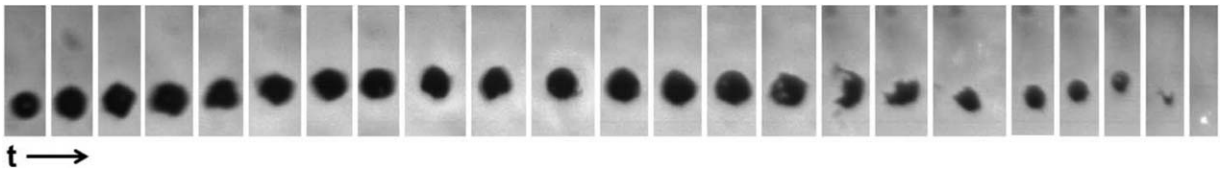

Figure 12. Image sequence of a 97-μm droplet composed of 0.5 mol/L Ce(III)2-ethylhexanoate in xylene burning in 0.4 L/min coflowing oxygen.

The time interval between each droplet image is 155μs, where t indicates the time succession.

deformations and oscillations of the droplet surface in the first images are the results of bubble growth and collapse. These deformations and swelling of the droplets have been also observed for slurry solutions. The time delay until disruption is shorter for Ce(III)2-EH compared to that for Sn(II)2-EH, which are not characterized by continuous deformation. Comparing the decomposition characteristics of Sn(II)2-EH and Ce(III)2-EH using thermogravimetric analysis (TGA) from room temperature to 1200°C under atmospheric air with a heating rate of 7.5°K/min (Figure S2 of Supporting Information), Ce(III)2-EH decomposes abruptly and over a wider range, than does Sn(II)2-EH. Although the heating rate during combustion is probably much faster, the TGA results indicate that the formation and accumulation of intermediates are more likely for Ce(III)2-EH due to the sudden decomposition steps and the wide range of decomposition temperature. Thus, Ce(III)2-EH should easily exceed the nucleation temperature of xylene and the boiling point of 2-EH acid. In contrast, Sn(II)2-EH decomposes within a narrow temperature range without incremental decomposition steps, perhaps explaining the different delay times until the onset of disruption, as well as the deformation and swelling of Ce(III)2-EH droplets. The shell of Ce(III)2-EH can attain higher temperatures due to the higher decomposition temperature, leading to fast nucleation. The wide and stepwise decomposition temperature of Ce(III)2-EH enables the continuous formation of intermediates that contribute to viscous shell creation. Such a viscous shell inhibits ejection due to nucleation and bubble growth, leading to the observed deformation and swelling of the Ce(III)2-EH solution.

However, Ce(III)2-EH contains more 2-EH acid than does Sn(II)2-EH. Therefore, if the time difference in the onset of disruption is due to the differing amounts of 2-EH acid in the solutions, the addition of 2-EH acid to the Sn(II)2-EH solution should result in a comparable time delay as for the Ce(III)2-EH solution. The behavior of a 0.5 mol/L Sn(II)2-EH solution, with additional 2-EH acid having the same amount of 2-EH acid as a 0.5 mol/L Ce(III)2-EH solution, is given in Figure 13. The additional amount of 2-EH acid delays the time until disruption compared to that for the original 0.5 mol/L Sn(II)2-EH solution, but is less than that for the xylene/2-EH acid solution. The droplet diameter and velocity evolutions of the 0.5 mol/L Sn(II)2-EH solution with additional 2-EH acid show an intermediate characteristic compared to those for the other solutions. It exhibits a similar change as the original 0.5 mol/L Sn(II)2-EH solution, but with a longer time delay. The velocity evolution shows that the 0.5 mol/L Sn(II)2-EH solution with additional 2-EH acid follows initially the curve of the 0.5 mol/L Sn(II)2-EH solution, but transitions to that of the xylene/2-EH acid solution. The same conclusions can be drawn from Figure 13b, where the Sn(II)2-EH solution with additional 2-EH acid burns as fast as the xylene/ 2-EH acid solution, but embodies a varying burning constant that resembles that of the 0.5 mol/L Sn(II)2-EH solution. These results demonstrate that the additional amount of 2-EH acid is not the reason for the rapid onset of disruption for the Ce(III)2-EH solution. Instead, the additional 2-EH acid dilutes the solution, delaying the buildup of a viscous shell and the onset of disruption. This illustrates the importance of the decomposition behavior of the metal precursor in the solution.

Combustion of Different Binary Xylene/Metal-2-EH Solutions

To further elucidate the disruptive combustion due to different decomposition characteristics, experiments are

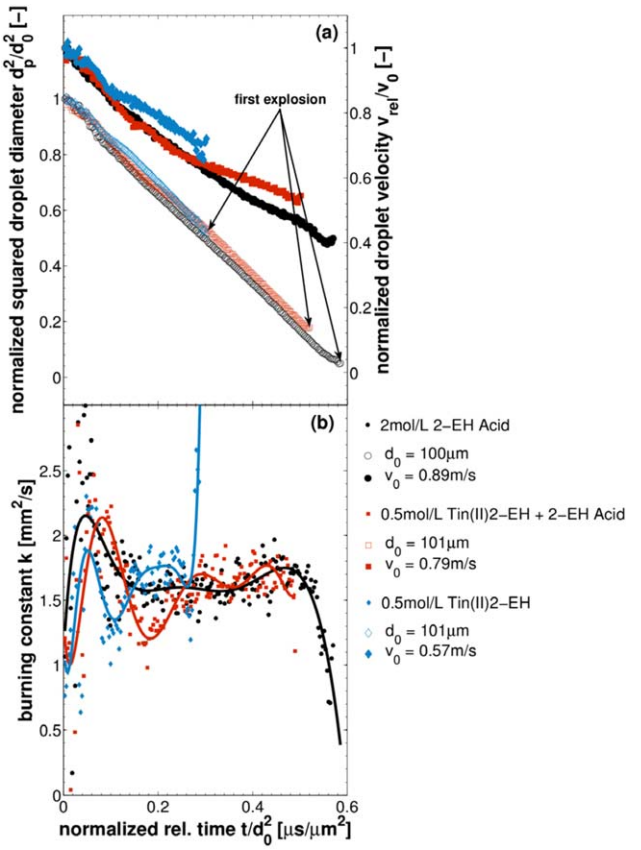

Figure 13. Evolution of (a) averaged normalized droplet diameter and velocity and (b) burning constant, for 2 mol/L 2-ethylhexanoic acid (○), 0.5 mol/L Sn(II)2-ethylhexanoate in xylene (◇), and 0.5 mol/L Sn(II)2-ethylhexanoate in xylene with additional 2-ethylhexanoic acid (□), burning in 0.4 L/min coflowing oxygen.

d_0 is the initial droplet diameter, and v_0 is the initial velocity. [Color figure can be viewed in the online issue, which is available at wileyonlinelibrary.com.]

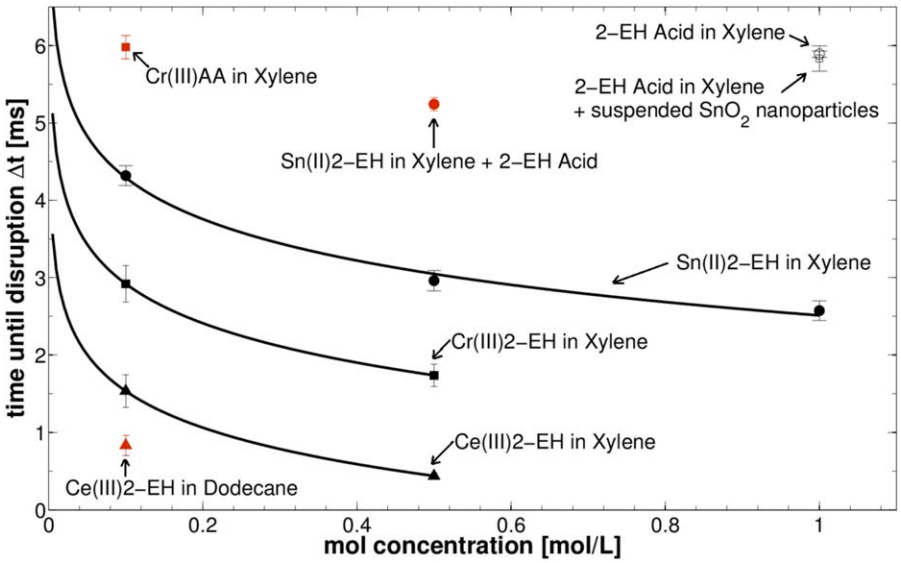

Figure 14. Average time delay between the ignition spark and the first explosion, for different solutions burning in 0.4 L/min coflowing oxygen.

[Color figure can be viewed in the online issue, which is available at wileyonlinelibrary.com.]

conducted with Ce(III)2-EH dissolved in dodecane, Cr(III)2-EH in xylene, and Cr(III)acetylacetonate (Cr(III)AA) in xylene. Because fast and disruptive combustion (especially of the Ce(III)2-EH and Cr(III)2-EH solutions) prohibits a suitable analysis of droplet size and velocity, the time between the spark and the first observed disruption (including deformation) is presented. The spark is taken as reference, instead of ignition, because is not always possible to observe a flame due to low soot tendency of the solutions. The ignition point has almost no influence on the burning behavior as has already been demonstrated in Figure 3. Figure 14 shows the time delay after the spark until the first droplet disruption, with respect to the molar concentration of the dissolved precursor. Only low concentrations of cerium and chromium are investigated, due to their high viscosities (e.g. up to η=47.7 mPa s for 1mol/L Cr(III)2-EH in Xylene). The small error bars in Figure 14 indicate that the time delay until disruption is highly reproducible, in fact suggesting heterogeneous nucleation. Since as soon as nucleation seeds are available, vapor nucleation of the high-volatile component will take place. In contrast, homogeneous nucleation has a stochastic nature and thus should be represented by appreciable scatter in the data.[77] The present data in Figure 14 do not show such stochastic nature. Homogeneous nucleation can be further ruled out with the Ce(III)2-EH in dodecane study, which shows faster onset of droplet disruption compared to xylene despite the higher homogeneous nucleation temperature of dodecane (T_{hn}=332 °C[78]), suggesting delayed vapor nuclei formation, that is, droplet disruption. These points together strongly indicate heterogeneous nucleation as a cause for the droplet disruption similar to that for slurry droplets.[73] The faster onset of disruption may be attributed to the higher viscosity of dodecane compared to that of xylene, which are η=1.48 mPa s and η=0.84 mPa s at 0.1 mol/L and 20°C, respectively. Because the liquid viscosity is inversely related to the diffusivity,[79] a twofold viscosity will roughly double the time needed for the molecules to diffuse through the solution. Such a cause would be in good agreement with the time delays until disruption, which are Δt=1.53 ms for xylene and Δt=0.83 ms for dodecane. However, comparing the 0.1 mol/L Ce(III)2-EH in dodecane solution with the 1 mol/L Sn(II)2-EH in xylene solution (η=1.56 mPa s at 1 mol/L and 20°C), which have approximately the same viscosities, the onset of disruption of the latter occurs with a much longer time delay. Another example is 0.5 mol/L Cr(III)2-EH in xylene solution (η=5.55 mPa s at 0.5 mol/L and 20°C) in comparison with 0.1 mol/L Ce(III)2-EH in xylene solution, which have significantly different viscosities, but approximately comparable time delays until explosion. Again, these results suggest that the disruptions are primarily due to the precursor characteristics and not to the solution viscosity. However, replacing a low-viscosity solvent with a high-viscosity solvent can promote droplet disruption by decreasing the diffusion of xylene through the viscous shell, affecting the vaporization rate. The onset of droplet disruption occurs sooner with increasing molar concentration of the corresponding 2-ethylhexanoate precursor. This similarity should be expected as all have the same precursor solvent. Moreover, note that the Ce(III)2-EH solutions always display the first onset of droplet disruption regardless of their concentration, followed by the Cr(III)2-EH and Sn(II)2-EH solutions, respectively. As the TGA data confirms, the decomposition curve of Cr(III)2-EH is between that of Sn(II)2-EH and Ce(III)2-EH, as their time until disruption suggests. Similar conclusion can be drawn from the 0.1mol/L Cr(III)AA solution, which disrupts only at the end of the observation limit, whereas the 0.1mol/L Cr(III)2-EH solution disrupts shortly after ignition. These results show that the actual bonding of the metal in the aerosol precursor, that is, decomposition characteristics, strongly influences the combustion of precursor/solvent droplets. As already described, this effect is in agreement with experimental results from FSP, where homogeneous nanoparticles are obtained for precursors that decompose more easily. Because the experiments suggest that droplet disruption takes place due to shell formation, which depends on the decomposition characteristics and concentration of the precursor, formation of

homogeneous nanoparticles in FSP are probably due to secondary atomization effects. This is similar to slurry droplets, where the surfactant properties control the disruptive combustion.

Summary

The combustion of aerosol precursors resembles those of slurry droplets, where the decomposition characteristics of the aerosol precursor significantly influence the burning of the droplets. Analogous to slurry fuels, the following mechanism for the combustion of droplets of aerosol precursor in solvent is proposed.

1. During the early stage of combustion, the high-volatile solvent will preferentially vaporize from a thin surface layer, leaving the low-volatile aerosol precursor in excess.
2. As combustion proceeds, a surface layer with the low-volatile aerosol precursor evolves, suppressing vaporization of the low-volatile solvent, leading to a flame contraction.
3. Because mass diffusion is slower than heat diffusion, the surface layer will quickly heat up as the flame moves closer to the droplet surface. Due to the higher boiling point of the low-volatile aerosol precursor, the temperature in the surface layer will increase, causing decomposition of the aerosol precursor, forming a variety of intermediates.
4. Although gaseous intermediates will be burned, liquid and solid intermediates can form a viscous shell, inhibiting vaporization while the temperature is still increasing.
5. Low-volatile solvent next to the shell and/or trapped in the shell during diffusion becomes superheated, forming vapor bubbles at the interface of the shell due to heterogeneous nucleation.
6. The pressure of the vapor bubbles will exceed the strength of the shell and disrupt the droplets and the shell.

In contrast to slurry droplets, where particles can build an impermeable shell, the behavior of the aerosol precursor droplets is mostly characterized by the d^2-law. The establishing layer and shell is inferred by the changes in the droplet velocity and burning constant. Depending on the decomposition characteristics of the aerosol precursor, (i.e., the formation of gaseous, liquid, and solid intermediates) a viscous shell is more or less formed. In general, disruption seems to be favored if the aerosol precursors decompose over a wide temperature range with incremental decomposition steps. Although the experiments already indicate that the combustion of aerosol precursor droplets differs significantly from the common model of distillation-like processes in the droplet-to-particle formation, additional investigations are necessary to predict the shell formation and breakage.

Acknowledgments

The authors would like to thank the Deutsche Forschungsgemeinschaft (DFG) for funding this project under grants of MA 3333/4-1. The authors also thank Andrej Gorzawski from the Department of Manufacturing Technologies (Foundation Institute of Material Science (IWT)—University of Bremen) for providing us with the high-speed camera and Torben Halfer from the Department of Advanced Ceramics (University of Bremen) for conducting the TGA measurements promptly.

Literature Cited

1. Pratsinis SE. Flame aerosol synthesis of ceramic powders. *Prog Energy Combust Sci*. 1998;24(3):197–219.
2. Mädler L, Kammler HK, Mueller R, Pratsinis SE. Controlled synthesis of nanostructured particles by flame spray pyrolysis. *J Aerosol Sci*. 2002;33(2):369–389.
3. Mädler L, Stark WJ, Pratsinis SE. Flame-made Ceria Nanoparticles. *J Mater Res*. 2002;17:1356–1362.
4. Teoh WY, Amal R, Mädler L. Flame spray pyrolysis: an enabling technology for nanoparticles design and fabrication. *Nanoscale*. 2010;2(8):1324–1347.
5. Strobel R, Pratsinis SE. Flame aerosol synthesis of smart nanostructured materials. *J Mater Chem*. 2007;17(45):4743–4756.
6. Pratsinis SE, Zhu W, Vemury S. The role of gas mixing in flame synthesis of titania powders. *Powder Technol*. 1996;86(1):87–93.
7. Briesen H, Fuhrmann A, Pratsinis SE. The effect of precursor in flame synthesis of SiO2. *Chem Eng Sci*. 1998;53(24):4105–4112.
8. Mädler L, Pratsinis SE. Bismuth oxide nanoparticles by flame spray pyrolysis. *J Am Ceram Soc*. 2002;85(7):1713–1718.
9. Tani T, Mädler L, Pratsinis SE. Homogeneous ZnO nanoparticles by flame spray pyrolysis. *J Nanopart Res*. 2002;4:337–343.
10. Heine MC, Pratsinis SE. Droplet and particle dynamics during flame spray synthesis of nanoparticles. *Ind Eng Chem Res*. 2005;44(16):6222–6232.
11. Gröhn AJ, Buesser B, Jokiniemi JK, Pratsinis SE. Design of turbulent flame aerosol reactors by mixing-limited fluid dynamics. *Ind Eng Chem Res*. 2011;50(6):3159–3168.
12. Gröhn AJ, Pratsinis SE, Wegner K. Fluid-particle dynamics during combustion spray aerosol synthesis of ZrO2. *Chemi Eng J*. 2012;191:491–502.
13. Jossen R, Pratsinis SE, Stark WJ, Mädler L. Criteria for flame-spray synthesis of hollow, shell-like, or inhomogeneous oxides. *J Am Ceram Soc*. 2005;88(6):1388–1393.
14. Strobel R, Pratsinis SE. Effect of solvent composition on oxide morphology during flame spray pyrolysis of metal nitrates. *Phys Chem Chem Phys*. 2011;13(20):9246–9252.
15. Spalding DB. The combustion of liquid fuels. *Symp (Int) Combust*. 1953;4(1):847–864.
16. Godsave GAE. Studies of the combustion of drops in a fuel spray - the burning of single drops of fuel. *Symp (Int) Combust*. 1953;4(1):818–830.
17. Goldsmith M, Penner SS. On the burning of single drops of fuel in a oxidizing atmosphere. *Jet Propulsion*. 1954;24:245–251.
18. Williams FA. On the assumptions underlying droplet vaporization and combustion theories. *J Chem Phys*. 1960;33(1):133–144.
19. Williams A. Combustion of droplets of liquid fuels: a review. *Combust Flame*. 1973;21(1):1–31.
20. Faeth GM. Current status of droplet and liquid combustion. *Prog Energy Combust Sci*. 1977;3(4):191–224.
21. Law CK. Recent advances in droplet vaporization and combustion. *Prog Energy Combust Sci*. 1982;8(3):171–201.
22. Law CK, Faeth GM. Opportunities and challenges of combustion in microgravity. *Prog Energy Combust Sci*. 1994;20(1):65–113.
23. Miyasaka K, Law CK. Combustion of strongly-interacting linear droplet arrays. *Symp (Int) Combust*. 1981;18(1):283–292.
24. Law CK, Chung SH, Srinivasan N. Gas-phase quasi-steadiness and fuel vapor accumulation effects in droplet burning. *Combust Flame*. 1980;38:173–198.
25. Bae JH, Avedisian CT. Nonane droplet combustion with and without buoyant convection: flame structure, burning rate and extinction in air and helium. *Proc Combust Inst*. 2009;32(2):2231–2238.
26. Balakrishnan P, Sundarajan T, Natarajan R. Combustion of a Fuel Droplet in a Mixed Convective Environment. *Combust Sci Technol*. 2001;163(1):77–106.
27. Ulmke H, Mietschke M, Bauckhage K. Piezoelectric single nozzle droplet generator for production of monodisperse droplets of variable diameter. *Chem Eng Technol*. 2001;24(1):69–70.
28. Riefler N, Wriedt T. Generation of monodisperse micron-sized droplets using free adjustable signals. *Part Part Syst Charact*. 2008;25(2):176–182.
29. Sangiovanni JJ, Labowsky M. Burning times of linear fuel droplet arrays: a comparison of experiment and theory. *Combust Flame*. 1982;47:15–30.
30. Randolph AL, Law CK. Influence of physical mechanisms on soot formation and destruction in droplet burning. *Combust Flame*. 1986;64(3):267–284.

31. Shaw BD, Dryer FL, Williams FA, Haggard Jr JB. Sooting and disruption in spherically symmetrical combustion of decane droplets in air. *Acta Astronaut*. 1988;17(11/12):1195–1202.
32. Law CK, Williams FA. Kinetics and convection in the combustion of alkane droplets. *Combust Flame*. 1972;19(3):393–405.
33. Sangiovanni JJ, Kesten AS. A theoretical and experimental investigation of the ignition of fuel droplets. *Combust Sci Technol*. 1977; 16(1–2):59–70.
34. Wong S-C, Liao X-X, Yang J-R. A simplified theory of the ignition of single droplets under forced convection. *Combust Flame*. 1997; 110(3):319–334.
35. He L, Tse SD, Law CK. Role of flamefront motion and criterion for global quasi-steadiness in droplet burning. *Symp (Int) Combust*. 1998;27(2):1943–1950.
36. Frenklach M. Reaction mechanism of soot formation in flames. *Phys Chem Chem Phys*. 2002;4(11):2028–2037.
37. Glassman I, Yetter RA. *Combustion*: Elsevier Inc., 2008;457–485.
38. Aldred JW, Williams A. The burning rates of drops of n-alkanes. *Combus Flame*. 1966;10(4):396–398.
39. Choi MY, Dryer FL, Haggard JB Jr. Observations on a slow burning regime for hydrocarbon droplets: n-Heptane/air results. *Symp (Int) Combust*. 1991;23(1):1597–1604.
40. Jackson GS, Avedisian CT, Yang JC. Observations of soot during droplet combustion at low gravity: heptane and heptane/monochloroalkane mixtures. *Int J Heat Mass Transf*. 1992;35(8):2017–2033.
41. Choi MY, Dryer FL, Green GJ, Sangiovanni JJ. Soot Agglomeration in Isolated, Free Droplet Combustion. *31st Aerospace Sciences Meeting: American Institute of Aeronautics and Astronautics*. 1993;823: 1–19.
42. Jackson GS, Avedisian CT. The effect of initial diameter in spherically symmetric droplet combustion of sooting fuels. *Proc Math Phys Sci*. 1994;446(1927):255–276.
43. Yozgatligil A, Park S-H, Choi MY, Kazakov A, Dryer FL. Influence of oxygen concentration on the sooting behavior of ethanol droplet flames in microgravity conditions. *Proc Combust Inst*. 2007;31(2): 2165–2173.
44. Park S-H, Choi S-C, Choi MY, Yozgatligil A. New observations of isolated ethanol droplet flames in microgravity conditions. *Combus Sci Technol*. 2008;180(4):631–651.
45. Park S-H, Choi MY. Formation of sootshell and attendant effects on droplet burning rate and radiative heat transfer in microgravity ethanol droplet flames. *Energy Fuels*. 2009;23(9):4395–4403.
46. Law CK, Xiong TY, Wang C. Alcohol droplet vaporization in humid air. *Int. J. Heat Mass Transf*. 1987;30(7):1435–1443.
47. Lee A, Law CK. An experimental investigation on the vaporization and combustion of methanol and ethanol droplets. *Combust Sci Technol*. 1992;86(1–6):253–265.
48. Shaw BD, Williams FA. Theory of influence of a low-volatility, soluble impurity on spherically-symmetric combustion of fuel droplets. *Int J Heat Mass Transf*. 1990;33(2):301–317.
49. Shaw BD. Studies of influences of liquid-phase species diffusion on spherically symmetric combustion of miscible binary droplets. *Combust Flame*. 1990;81:277–288.
50. Shaw BD, Aharon I, Lenhart D, Dietrich DL, Williams FA. Spacelab and drop-tower experiments on combustion of methanol/dodecanol and ethanol/dodecanol mixture droplets in reduced gravity. *Combust Sci Technol*. 2001;167(1):29–56.
51. Dee V, Shaw BD. Combustion of propanol-glycerol mixture droplets in reduced gravity. *Int J Heat Mass Transf*. 2004;47(22):4857–4867.
52. Eisenklam P, Arunachalam SA, Weston JA. Evaporation rates and drag resistance of burning drops. *Symp (Int) Combust*. 1967;11(1): 715–728.
53. Chuchottaworn P, Asano K. Calculation of drag coefficients of an evaporating or a condensing droplet. *J Chem Eng Japan*. 1985;18(1): 91–94.
54. Asano K, Taniguchi I, Maeda K, Kosuge H. Simultaneous measurement of drag coefficients and mass transfer of a volatile drop falling freely. *J Chem Eng Japan*. 1988;21(4):387–393.
55. Dwyer HA, Sanders BR. A detailed study of burning fuel droplets. *Symp (Int) Combust*. 1988;21(1):633–639.
56. Nakaya S, Fujishima K, Tsue M, Kono M, Segawa D. Effects of droplet diameter on instantaneous burning rate of isolated fuel droplets in argon-rich or carbon dioxide-rich ambiences under microgravity. *Proc Combust Inst*. 2013;34(1):1601–1608.
57. Lefebvre AH. *Atomization and Sprays*. Taylor & Francis, 1989;201–266.
58. Law CK. Internal boiling and superheating in vaporizing multicomponent droplets. *AIChE J*. 1978;24(4):626–632.
59. Randolph AL, Makino A, Law CK. Liquid-phase diffusional resistance in multicomponent droplet gasification. *Symp (Int) Combust*. 1988;21(1):601–608.
60. Zhang H, Law CK. Effects of temporally varying liquid-phase mass diffusivity in multicomponent droplet gasification. *Combust Flame*. 2008;153(4):593–602.
61. Mishra S, Daniele S, Hubert-Pfalzgraf LG. Metal 2-ethylhexanoates and related compounds as useful precursors in materials science. *Chem Soc Rev*. 2007;36(11):1770–1787.
62. Blander M, Katz JL. Bubble nucleation in liquids. *AIChE J*. 1975; 21(5):833–848.
63. Fletcher NH. Size Effect in Heterogeneous Nucleation. *J Chem Phys*. 1958;29(3):572–576.
64. Lasheras JC, Fernandez-Pello AC, Dryer FL. Experimental observations on the disruptive combustion of free droplets of multicomponent fuels. *Combust Sci Technol*. 1980;22(5–6):195–209.
65. Zhao Y, Dong G, Duan L, Qiao J, Zhang D, Wang L, Qui Y. Impacts of Sn precursors on solution-processed amorphous zinc-tin oxide films and their transistors. *RSC Adv*. 2012;2(12):5307–5313.
66. Vest RW. Metallo-organic decomposition (MOD) processing of ferroelectric and electro-optic films: a review. *Ferroelectrics*. 1990; 102(1):53–68.
67. Galembeck A, Alves OL. BiVO4 thin film preparation by metalorganic decomposition. *Thin Solid Films*. 2000;365(1):90–93.
68. Gross ME, Gallagher PK, Brown WL. Superconducting thin films and ion beam patterning using metal carboxylate precursors. *Solid State Ionics*. 1989;32–33(2):1051–1055.
69. Shen W-N, Dunn B, Moore CD, Goorsky MS, Radetic T, Gronsky R. Synthesis of nanoporous bismuth films by liquid-phase deposition. *J Mater Chem*. 2000;10(3):657–662.
70. Takahashi F, Dryer FL, Williams FA. Combustion behavior of free boron slurry droplets. *Symp (Int) Combust*. 1988;21(1):1983–1991.
71. Takahashi F, Heilweil IJ, Dryer FL. Disruptive burning mechanism of free slurry droplets. *Combust Sci Technol*. 1989;65(1–3):151–165.
72. Wong SC, Turns SR. Disruptive burning of aluminum-carbon slurry droplets. *Combust Sci Technol*. 1989;66(1–3):75–92.
73. Wong S-C, Lin A-C, Chi H-Y. Effects of surfactant on the evaporation, shell formation and disruptive behavior of slurry droplets. *Symp (Int) Combust*. 1991;23(1):1391–1397.
74. Wong S-C, Lin A-C, Wu C-E. Microexplosions of boron and boron-carbon slurry droplets. *Combust Flame*. 1994;96(3):304–310.
75. Byun DY, Baek SW, Cho JH. Microexplosion of aluminum slurry droplets. *Int J Heat Mass Transf*. 1999;42(24):4475–4486.
76. Ben-Dor G, Elperin T, Krasovitov B. Effect of thermo- and diffusiophoretic forces on the motion of flame-generated particles in the neighbourhood of burning droplets in microgravity conditions. *Proc Math Phys Eng Sci*. 2003;459(2031):677–703.
77. Mikami M, Kojima N. An experimental and modeling study on stochastic aspects of microexplosion of binary-fuel droplets. *Proc Combust Inst*. 2002;29(1):551–559.
78. Eberhart JG, Kremsner W, Blander M. Metastability limits of superheated liquids: Bubble nucleation temperatures of hydrocarbons and their mixtures. *J Colloid Interface Sci*. 1975;50(2):369–378.
79. Hayduk W, Cheng SC. Review of relation between diffusivity and solvent viscosity in dilute liquid solutions. *Chem Eng Sci*. 1971; 26(5):635–646.
80. Lide DR. *CRC Handbook of Chemistry and Physics*, *84th Edition*: CRC Press, 2003;6-111/119/120/122, 8-104/105/108.

Manuscript received Apr. 22, 2013, and revision received Sept. 3, 2013.